© 2019. Published by The Company of Biologists Ltd | Development (2019) 146, dev183780. doi:10.1242/dev.183780

RESEARCH ARTICLE

The plakin domain of *C. elegans* VAB-10/plectin acts as a hub in a mechanotransduction pathway to promote morphogenesis

Shashi Kumar Suman[1,2], Csaba Daday[3,4], Teresa Ferraro[1], Thanh Vuong-Brender[1,2,*], Saurabh Tak[1,2], Sophie Quintin[2], François Robin[1], Frauke Gräter[3,4] and Michel Labouesse[1,2,‡]

ABSTRACT

Mechanical forces can elicit a mechanotransduction response through junction-associated proteins. In contrast to the wealth of knowledge available for focal adhesions and adherens junctions, much less is known about mechanotransduction at hemidesmosomes. Here, we focus on the *C. elegans* plectin homolog VAB-10A, the only evolutionary conserved hemidesmosome component. In *C. elegans*, muscle contractions induce a mechanotransduction pathway in the epidermis through hemidesmosomes. We used CRISPR to precisely remove spectrin repeats (SRs) or a partially hidden Src homology 3 (SH3) domain within the VAB-10 plakin domain. Deleting the SH3 or SR8 domains in combination with mutations affecting mechanotransduction, or just the part of SR5 shielding the SH3 domain, induced embryonic elongation arrest because hemidesmosomes collapse. Notably, recruitment of GIT-1, the first mechanotransduction player, requires the SR5 domain and the hemidesmosome transmembrane receptor LET-805. Furthermore, molecular dynamics simulations confirmed that forces acting on VAB-10 could make the central SH3 domain, otherwise in contact with SR4, available for interaction. Collectively, our data strongly indicate that the plakin domain plays a central role in mechanotransduction and raise the possibility that VAB-10/plectin might act as a mechanosensor.

KEY WORDS: *C. elegans*, Hemidesmosome, Mechanotransduction, Morphogenesis, Spectraplakin, Spectrin repeat

INTRODUCTION

Cells are constantly exposed to various mechanical forces, and their ability to respond is crucial for tissue homeostasis, particularly in the context of morphogenesis and cancer progression. For example, during tissue and organ formation, epithelial tissues become strongly deformed due to both cell-intrinsic and cell-extrinsic forces (Gilmour et al., 2017). Mechanical forces can be instructive, as when deformation of one organ influences morphogenesis of neighbouring organs (Aigouy et al., 2010; Collinet et al., 2015; Lye et al., 2015). Yet cells within the epithelium must maintain cell-cell and cell-matrix cohesion. The adaptation process to these forces relies on mechanosensing and the transduction of specific signals from junctions to the cytoskeleton or to the nucleus (Iskratsch et al., 2014; Ladoux et al., 2015).

Focal adhesions and adherens junctions play a central role in relaying mechanical forces. Tension exerted on those junctions result in conceptually similar effects, whereby a protein acting as a junction-linked mechanosensor is unfolded and recruits additional proteins, which either strengthen the junction or induce biochemical signalling (Chen et al., 2017; Moore et al., 2010). Typically, tension applied to focal adhesions can unfold talin, which then recruits vinculin (del Rio et al., 2009) or the adaptor p130Cas, which subsequently activates the small GTPase Rap1 (Sawada and Sheetz, 2002; Sawada et al., 2006). Likewise, α-catenin acts as an adherens junction mechanosensor that also recruits vinculin to strengthen the junction (le Duc et al., 2010; Yao et al., 2014; Yonemura et al., 2010).

Hemidesmosomes represent another mechano-sensitive junction about which much less is known. In *C. elegans*, we previously found that the hemidesmosome-like junction present in epidermal cells transmits mechanical tension exerted by muscles when they contract (Zhang et al., 2011). *C. elegans* muscles are positioned along the anterior-posterior axis under the dorso-ventral epidermis (see cross-hatched red lines in Fig. 1A,A′). They are tightly connected to the epidermis through a complex structure acting as trans-epithelial tendons, called fibrous organelles, consisting in two hemidesmosome-like junctions (CeHDs) connected by intermediate filaments (Fig. 1B) (Francis and Waterston, 1991; Gieseler et al., 2017; Vuong-Brender et al., 2016). These structures include the plectin homologue VAB-10A and intermediate filaments in common with the canonical vertebrate hemidesmosome (Zhang and Labouesse, 2010). Owing to this tight connection, when muscles contract, they transmit mechanical tension to dorsal and ventral epidermal cells. This, in turn, initiates a mechanotransduction process in the dorsal and ventral epidermal cells that require functional hemidesmosomes (Fig. 1A-B) (Zhang et al., 2011), and induces the reorganization of actin filament bundles in the epidermis (Lardennois et al., 2019). We have previously found that the first detectable step in this mechanotransduction process corresponds to the recruitment of the adaptor protein GIT-1 to hemidesmosomes (Fig. 1C) (Zhang et al., 2011). Although VAB-10A/plectin is essential for hemidesmosome integrity (Bosher et al., 2003), its potential role in the mechanotransduction process had not been investigated. In vertebrates, plectin, a core component of vertebrate hemidesmosomes, interacts with dystroglycan to mediate mechano-signalling in lung epithelial cells, independently of hemidesmosomes, in a process leading to ERK1/2 and AMPK activation (Takawira et al., 2011). Plectin is also important for maintaining the nuclear shape of keratinocytes as they adhere and spread out on micropatterns, which they do by regulating the density of the perinuclear keratin meshwork and through a negative regulation of MAPK activity; as such it regulates nuclear mechanotransduction (Almeida et al., 2015).

[1]Sorbonne Université, CNRS, Institut de Biologie Paris Seine, Laboratoire de Biologie du Développement/UMR7622,7 Quai St-Bernard, 75005 Paris, France. [2]Development and Stem Cells Program, IGBMC, CNRS (UMR7104), INSERM (U964), Université de Strasbourg, 1 rue Laurent Fries, BP10142, 67400 Illkirch, France. [3]Interdisciplinary Center for Scientific Computing (IWR), Heidelberg University, Mathematikon, INF 205, 69120 Heidelberg, Germany. [4]Heidelberg Institute for Theoretical Studies, Schloß-Wolfsbrunnenweg 35, 69118 Heidelberg, Germany.
*Present address: Cell Biology Division, MRC-LMB, Cambridge CB2 0QH, UK.

‡Author for correspondence (michel.labouesse@upmc.fr)

M.L., 0000-0001-7995-5843

Received 13 August 2019; Accepted 18 November 2019

Development (2019) 146, dev183780. doi:10.1242/dev.183780

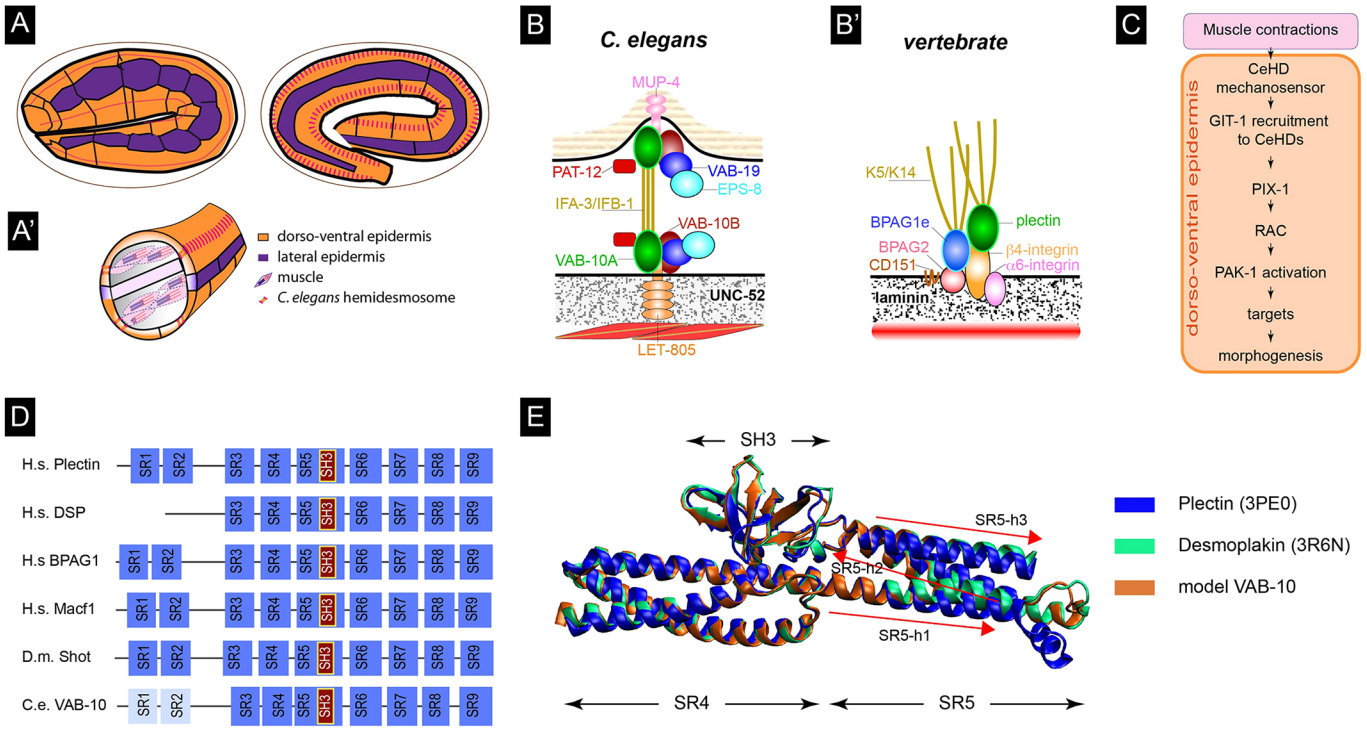

Fig. 1. The SR4-SR5-SH3 domains of plectin and VAB-10 have a similar conformation. (A) Muscles are required for the embryo to elongate from the twofold stage (left) to the terminal fourfold/pretzel stage (right). (A′) Cross-section of the embryo showing the relative positions of muscles and epidermal cells. (B) Comparison of the embryonic *C. elegans* and (B′) vertebrate hemidesmosome junctions. The drawing is only showing essential *C. elegans* hemidesmosome proteins (GIT-1, PIX-1 and PAK-1 are not included). Besides intermediate filaments, the only evolutionary conserved proteins are plakins: plectin and BPAG1e in vertebrates; and VAB-10A in *C. elegans* (green; the VAB-10B/MACF plakin transiently associates with the hemidesmosome). LET-805 basally, MUP-4 apically and the intermediate filament dimers IFA-3/IFB-1 and PAT-12 are nematode-specific proteins. VAB-19 and its binding partner EPS-8B have homologs in vertebrates (Kank1 and EPS8, respectively) that are not known to associate with vertebrate hemidesmosomes. The basal ECM ligand UNC-52 is homologous to perlecan, whereas the apical ligand includes several proteins with zona pellucida domains. (C) Outline of the mechanotransduction pathway occurring in the epidermis in response to the tension created by the contraction of muscles, which are tightly linked to the epidermis. (D) Comparison of the plakin domain of plectin and spectraplakins, showing that all of them have a predicted SH3 domain nested within a spectrin domain. The structure prediction is based on previous work (Choi and Weis, 2011; Daday et al., 2017; Ortega et al., 2016) and on BLASTP alignments. Numbering of the SR domains is based on plectin in this and all subsequent figures (Ortega et al., 2011, 2016). (E) 3D structure of the SH3 and surrounding spectrin repeats from human plectin (PDB 3PE0; blue), human desmoplakin (PDB 3R6N; green) and superimposed Pymol prediction for the homologous spectrin repeat and SH3 domain from VAB-10 (orange). The only major difference between them is in the minor helix on the right.

VAB-10 and plectin belong to the spectraplakin family, which are large proteins linking different cytoskeleton networks. They include an N-terminal actin-binding domain (calponin homology); a plakin domain consisting of up to nine spectrin repeats (SR) with an atypical Src homology 3 (SH3) domain found within the central SR (either multiple spectrin or plectin repeats); and a C-terminal microtubule-binding domain (Zhang et al., 2017). Each SR comprises three α-helices; the SH3 domain bulges out of the loop connecting the second and third α-helices of SR5 (Choi and Weis, 2011; Ortega et al., 2011). Vertebrate desmopklakin, envoplakin, periplakin and plectin represent a spectraplakin subfamily known as plakins; the first three lack the actin- and microtubule-binding domains, but carry plectin repeats (Sonnenberg and Liem, 2007). The goal of the present work was to examine whether VAB-10A is required to mediate the mechanotransduction response triggered in epidermal cells by muscles. We sought to determine the domains that could mediate this response, by removing specific domains within VAB-10 using a CRISPR/Cas9 approach. Our data reveal a key role for an SH3 protein-protein interaction domain and its spectrin repeat shield in mediating mechanotransduction. As VAB-10A/plectin is the only hemidesmosomal protein conserved between *C. elegans* and vertebrates (Zhang and Labouesse, 2010), it is likely that responses gained from *C. elegans* will apply to vertebrate hemidesmosomes.

RESULTS

Isolation of novel SH3 and spectrin repeat mutations in *vab-10*

Proteins found at *C. elegans* hemidesmosomes are detailed in Fig. 1B. As outlined above, VAB-10A is the only conserved hemidesmosome protein between *C. elegans* and vertebrates (Zhang and Labouesse, 2010) – the gene *vab-10* produces two major isoforms through alternative splicing, VAB-10A/plectin and VAB-10B/MACF, which have the N-terminal actin-binding domain and the plakin domain in common (see below) (Bosher et al., 2003). Several considerations prompted us to focus more specifically on the potential role of the central plakin domain. First, this domain is well conserved among plakin and spectraplakin families such as vertebrate desmoplakin, plectin and MACF/ACF7, *Drosophila* Shot and *C. elegans* VAB-10 (Zhang et al., 2017). Interestingly, SRs such as those present within the plakin domain are known to unfold *in vitro* under mechanical stress (Law et al., 2003; Lenne et al., 2000). Second (Fig. 1D), although the SH3 domain present within SR5 lacks some critical residues compared with canonical SH3 domains, questioning its ability to interact with Pro-rich regions, its

Development (2019) 146, dev183780. doi:10.1242/dev.183780

evolutionary conservation suggests that it could still link specific ligands when exposed (Choi and Weis, 2011; Ortega et al., 2011). The crystal structure of that region from desmoplakin and plectin suggests that the SH3 domain interacts with the upstream spectrin repeat to stabilize the plakin domain, which should make the SH3 binding region partially occluded and prevented from interacting with other proteins (Fig. 1E) (Choi and Weis, 2011; Ortega et al., 2011). Third, recent molecular dynamics simulations (MDSs) on plectin and desmoplakin suggested that mechanical force should unfold the two neighbouring spectrin repeats to unmask the SH3 domain (Daday et al., 2017).

We first modelled the equivalent region of VAB-10 on top of human plectin, which showed that its SH3 domain should also be involved in making contacts with the upstream SR4 repeat (Fig. 1E). To functionally test the importance of the plakin domain, we engineered several mutations in *vab-10* by CRISPR-mediated recombination (Fig. 2A,B). Specifically, we introduced a deletion of the first two α-helices within the SR5 preceding the SH3 domain, named *vab-10(mc64)* or *vab-10(ΔSR5h1-h2)*; a deletion of the entire SH3 domain named *vab-10(mc62)* or *vab-10(ΔSH3)*; deletions removing SR7 or SR8, named *vab-10(mc97)* and *vab-10(mc98)*, respectively (or Δ*SR7* and Δ*SR8*); a deletion of the SH3 PSVV residues contributing to ligand binding among canonical SH3 domains, named *vab-10(mc56)*; and several point mutations in conserved SH3 residues or in a cysteine of SR4 predicted to interact with the SH3 domain (Fig. 2A,B, Fig. S1). Our attempts to isolate similar deletions of the other SR domains were unfortunately unsuccessful. By comparison with previously known *vab-10* alleles, *vab-10(ΔSR5h1-h2)* behaved like a strong *vab-10* allele, segregating 100% dead embryos that elongated slightly beyond the twofold stage (Fig. 2C-D, Table 1). By contrast, over 90% of animals homozygous for *vab-10(ΔSH3)*, deletion of the SH3 PSVV residues *vab-10(ΔSR7)* and *vab-10(ΔSR8)* were normal, with a few late embryo/arrested larvae displaying a very lumpy morphology (Fig. 2E-G). Other point mutations were homozygous viable with no apparent phenotype (Fig. 2I; Table S1). In the remainder of this study, we will mainly focus on the SH3 deletion, SR8 deletion and on the deletion removing the two SR5 α-helices

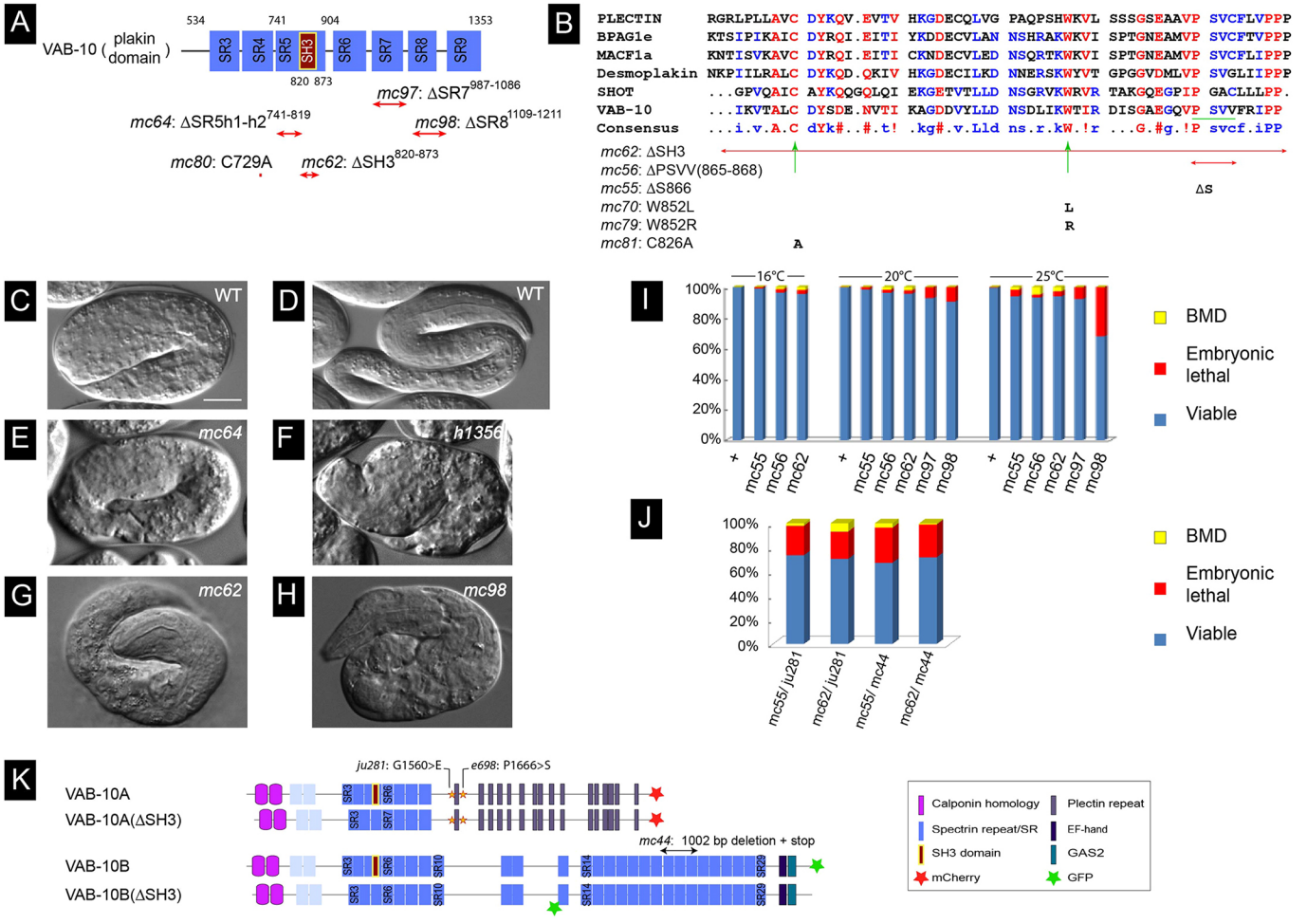

Fig. 2. The SR5 and SH3 domains of VAB-10 are important for embryonic elongation. (A) Positions of the CRISPR-generated mutations in the plakin domain. (B) Alignment of the SH3 domain among spectraplakins and plakins (as predicted by the Clustal Omega software), along with the positions of the residues mutated by CRISPR. (C-H) DIC micrographs of a wild-type twofold embryo (C) and young L1 hatchling (D), an arrested *mc64* (noted Δ*SR5h1-h2* in the text) embryo (E), a *h1356* embryo that is a presumptive *vab-10* null allele (F), a rare malformed *mc62* embryo (noted Δ*SH3* in the text) (G), and a rare malformed *mc98* embryo (Δ*SR8* in the text) (H). (I) Quantification of the embryonic and larval lethality rates among the main new *vab-10* alleles (see also Table 1). (J) Allelic complementation tests between *mc55* or *mc62* and the very strong *vab-10A(ju281)* and *vab-10B(mc44)* alleles; the phenotypes correspond to those observed in the progeny of *mc62*/*ju281* and *mc62*/*mc44* trans-heterozygous adults. χ^2 analysis shows the distributions are not statistically different. (K) The VAB-10A and VAB-10B isoforms were tagged with mCherry and GFP, respectively. Additionally, these markers were introduced in a *vab-10(ΔSH3)* mutant, except that the GFP could not be obtained at the C terminus for *vab-10B(ΔSH3)*. Scale bar: 10 µm.

Table 1. Phenotype rates of mutations affecting the VAB-10 plakin domain

A. Lethality of novel *vab-10* alleles

Genotype*	Viable	EL	BMD	*n*
Wild type	98.7%	1.3%	0.0%	2663
vab-10A::mCherry=vab-10(mc100)	98.3%	1.7%	0.0%	1098
vab-10[SH3(ΔS866)]=vab-10(mc55)	98.6%	1.4%	0.0%	1109
vab-10[SH3(ΔPSVV_865-868)]=vab-10(mc56)	96.3%	2.2%	1.5%	1152
vab-10(ΔSH3)=vab-10(mc62)	91.1%	8.4%	0.5%	2432
vab-10[SH3(W852L)]=vab-10(mc70)	99.5%	0.5%	0.0%	982
vab-10[SH3(W852R)]=vab-10(mc79)	99.4%	0.6%	0.0%	1034
vab-10[SR4(C729A)]=vab-10(mc80)	98.0%	2.0%	0.0%	1304
vab-10[SH3(C826A)]=vab-10(mc81)	98.7%	1.3%	0.0%	937
vab-10A(ΔSH3)::mCherry=vab-10(mc109)	92.4%	6.8%	0.8%	1178
vab-10(ΔSR5h1-h2)=vab-10(mc64)	0.0%	100%	0.0%	984[§]
vab-10(ΔSR7)=vab-10(mc97)	96.8%	3.2%	0.0%	1494
vab-10(ΔSR8)=vab-10(mc98)	95.9%	3.7%	0.4%	1125

B. Genetic interactions between *vab-10(ΔSH3)* and genes known to interact with *vab-10A(e698)*

	Wild type				*vab-10(e698)*				*vab-10(ΔSH3)*			
Genotype*	Viable	EL	BMD	*n*	Viable	EL	BMD	*n*	Viable	EL	BMD	*n*
pak-1(RNAi)	99.1%	0.6%	0.3%	1423	98.5%	1.5%	0.0%	1029	0.9%	99.1%	0.0%	1336
pak-1(ok448)	98.4	1.2%	0.4%	1296	-	-	-	-	0.0%	100%	0.0%	1423[§]
pak-1(tm403)	96.4%	3.6%	0.0%	1410	-	-	-	-	35.6%	43.4%	21.0%	1680
git-1(tm1962)	98.1%	1.9%	0.0%	1752	-	-	-	-	2.0%	98.0%	0.0%	1345
crt-1(RNAi)	99.0%	1.0%	0.0%	724	52.4%	46.9%	0.7%	531	57.0%	11.0%	32.0%	537
mec-8(RNAi)	97.4%	2.6%	0.0%	778	62.2%	34.7%	3.1%	584	55.3%	39.3%	5.4%	628

C. Genetic interactions of novel *vab-10* alleles and *pak-1*

	vab-10[SH3(W852L)]				*vab-10[SH3(W852R)]*				*vab-10[SR4(C729A)]*				*vab-10(mc56)*				*vab-10(ΔSR7)*				*vab-10(ΔSR8)*			
Genotype*	Viable	EL	BMD	*n*	Viable	EL	BMD	*n*	Viable	EL	BMD	*n*	Viable	EL	BMD	*n*	Viable	EL	BMD	*n*	Viable	EL	BMD	*n*
pak-1(RNAi)	-	-	-	-	-	-	-	-	-	-	-	-	27.2%	46.2%	26.7%	-	95.4%	4.6%	0.0%	936	10.8%	50.5%	39.1%	848
pak-1(ok448)	99.8%	0.2%	0.0%	767	99.8%	0.2%	0.0%	745	99.8%	0.2%	0.0%	620	-	-	-	1423[§]	67.0%	5.9%	27.1%	578	0.0%	100%	0.0%	736
pak-1(tm403)	99.5%	0.3%	0.2%	716	99.7%	0.3%	0.0%	675	-	-	-	-	-	-	-	-	-	-	-	-	-	-	-	

*Viability judged 24 h after egg-laying.
[§]Numbers correspond to the total progeny of the relevant heterozygous balanced strains.
BMD, important body morphology defects; EL, embryonic lethality.

Development (2019) 146, dev183780. doi:10.1242/dev.183780

Development (2019) 146, dev183780. doi:10.1242/dev.183780

preceding the SH3 domain, and briefly mention the results obtained with other mutants.

To test whether the *vab-10(ΔSH3)* mutation affects the *vab-10A* or *vab-10B* isoforms, we performed complementation tests with the embryonic lethal alleles *vab-10A(ju281)* and *vab-10B(mc44)* (see Fig. 2K for their positions). Assuming that *vab-10(ΔSH3)* disrupts a specific *vab-10* isoform, then the corresponding trans-heterozygous combination should not be viable or should display serious larval defects, whereas the other trans-heterozygous combination should be normal. In contrast to what we had previously observed when testing the complementation between *vab-10A(e698)* and other *vab-10* alleles (Bosher et al., 2003), we could establish trans-heterozygous *vab-10A(ju281)/vab-10ΔSH3)* and *vab-10B(mc44)/vab-10(ΔSH3)* animals that both segregated between 23% and 29% embryonic lethality and up to 7% strong larval body morphology defects (Fig. 2J) – *vab-10A(e698)* affects a non-conserved region of the protein (Fig. 2K). As homozygous *vab-10A(ju281)* or *vab-10B(mc44)* represent 25% of the progeny, and homozygous *vab-10(ΔSH3)* another 25% of the progeny, among which fewer than 10% display strong defects (see Table 1, Fig. 2I), we conclude that *vab-10(ΔSH3)* does not severely compromise VAB-10 function. Furthermore, the distribution of the different categories was not statistically different in the progeny of *ju281/mc62* versus *mc44/mc62* trans-heterozygotes. Hence, this complementation test alone does not reveal whether *vab-10(ΔSH3)* is a *vab-10A* or *vab-10B* allele, or possibly whether both isoforms might fulfil the function provided by the SH3 domain during embryonic elongation.

To facilitate the study of VAB-10, we also generated a CRISPR knock-in of the VAB-10A isoform marked by mCherry at its C terminus as well as a ΔSH3 version of this knock-in; likewise, we generated a CRISPR knock-in of the other major isoform VAB-10B marked by GFP at the C terminus for the wild-type form, and internally before its SR13 for the ΔSH3 form (Fig. 2I). Homozygous VAB-10A::mCherry and VAB-10B::GFP animals were normal, whereas their ΔSH3 derivatives behaved like *vab-10(ΔSH3)* animals, segregating as <10% arrested embryos or L1 larvae (Table 1).

The VAB-10A plakin domain is essential for mechanotransduction

We had previously found that mutations in *git-1* or *pak-1* induce high levels of embryonic lethality when combined with the weak allele *vab-10A(e698)*, resulting in compromised hemidesmosomes (Zhang et al., 2011). We thus tested whether double mutants of *vab-10(ΔSH3)* or *vab-10(ΔSR8)* and *git-1(tm1962)* or *pak-1(ok448)* would induce a similar phenotype. Strikingly, time-lapse DIC microscopy of *vab-10(ΔSH3); pak-1(ok448)*, *vab-10(ΔSH3); git-1(tm1962)* or *vab-10(ΔSR8); pak-1(ok448)*, and to a lesser extent *vab-10(ΔSH3); pak-1(tm403), vab-10(mc56); pak-1(RNAi)* or *vab-10(ΔSR8); pak-1(RNAi)*, embryos showed that most of them did not progress beyond the 2.5-fold stage (Fig. 3A-C; Movies 1-3). Specifically, 98% of *vab-10(ΔSH3); git-1(tm1962)*, 100% *vab-10(ΔSH3)*; *pak-1(ok448)* and *vab-10(ΔSR8); pak-1(ok448)* embryos failed to hatch (Table 1, Fig. 3B), underlining a strong synergistic effect between mutations that have on their own very weak embryonic defects. The allele *pak-1(ok448)* is a presumptive null, with no kinase domain, whereas the allele *tm403* lacks the GTPase-binding domain of PAK-1. These double mutants elongated at a wild-type rate until the 2.2-fold stage, then arrested (Fig. 3A,C). We also observed ∼50% lethality after RNAi against *mec-8* or *crt-1* in the *vab-10(ΔSH3)* background, two strong enhancers of *vab-10A(e698)* without an embryonic phenotype of their own (Zahreddine et al., 2010) (Table 1). These genetic interactions, together with the type of embryonic arrest, strongly support the notion that *vab-10(ΔSH3)* and *vab-10(ΔSR8)* behave like *vab-10A* alleles. Hence, based on genetic interactions with genes known to mediate mechanotransduction, the SH3 and SR8 domains are important for mechanotransduction. We could also observe a milder genetic interaction between *vab-10(ΔSR7)* and *pak-1(ok448)* (Fig. S1; Table 1), potentially suggesting that a larger part of the VAB-10 plakin domain is important for mechanotransduction.

The VAB-10A plakin domain contributes to maintain hemidesmosome integrity

We had previously found that hemidesmosomes fall apart in most *vab-10A(e698); pak-1(ok448)* double-mutants (Zhang et al., 2011). To define whether embryos with plakin domain mutations had arrested elongation for similar reasons, we examined the distribution of LET-805::GFP and MUP-4::GFP, the basal and apical hemidesmosome receptors, respectively. For this, we generated knock-in versions of MUP-4::GFP and LET-805::GFP. After PAK-1 knockdown in the *vab-10A(ΔSH3)::mCherry* or *vab-10(ΔSR8)* backgrounds (Fig. 4A), basal LET-805::GFP hemidesmosomes were normal until the twofold stage, and then displayed integrity defects mainly in the region where embryo curvature is the highest (Fig. 4A and Movies 4 and 5; see arrows and dotted line in Fig. 4A). Specifically, the LET-805::GFP signal appeared to detach from the outer body wall and to collapse internally as if no longer connected in *vab-10(ΔSH3)* mutants, consistent with the observation that muscles also detached from the body wall (Fig. S2). The basal VAB-10(mc62)::mCherry signal remained associated with it, but was much dimmer, suggesting that detachment occurred within the epidermis layer (Fig. 4B, bottom three rows and Movie 6). By contrast, at the apical side, the signal appeared intense although often less compact (Fig. 4B). These defects, which were not observed in VAB-10A(+)::mCherry control embryos after PAK-1 knockdown (Fig. 4B upper row), are strongly reminiscent of those previously observed in *vab-10A(e698); pak-1(ok448)* double mutants (Zhang et al., 2011). Interestingly, the same LET-805::GFP detachment phenotype was observed in *vab-10(ΔSR5h1-h2)* embryos (Fig. 4C). However, in contrast to the situation observed in embryos homozygous for the presumptive null allele *vab-10(h1356)* (Bosher et al., 2003), LET-805 could still be observed in the remainder of the embryo, arguing that *vab-10(ΔSR5h1-h2)* is only a hypomorph. The apical hemidesmosome receptor MUP-4::GFP was also affected at the turn of the embryos and displayed a much fainter intensity (Fig. 4D). These results and the aforementioned genetic interactions strengthen our conclusion that the SH3 and SR8 domains within the VAB-10A/plectin isoform are acting in the mechanotransduction process to enable hemidesmosomes to sustain tension beyond the twofold stage. This does not preclude an additional role for these domains within the VAB-10B/MACF isoform. We suggest that hemidesmosomes preferentially rupture in the most convex part of the embryo because tension is higher where the curvature is higher.

GIT-1 recruitment to hemidesmosomes depends on VAB-10 and LET-805

We have previously established that GIT-1 recruitment to hemidesmosomes is the first detectable step in the mechanotransduction pathway (Fig. 1C). One possibility is that a hemidesmosome-associated protein (or proteins) acting as a mechanosensor is able to sense changes in tension when muscles

Development (2019) 146, dev183780. doi:10.1242/dev.183780

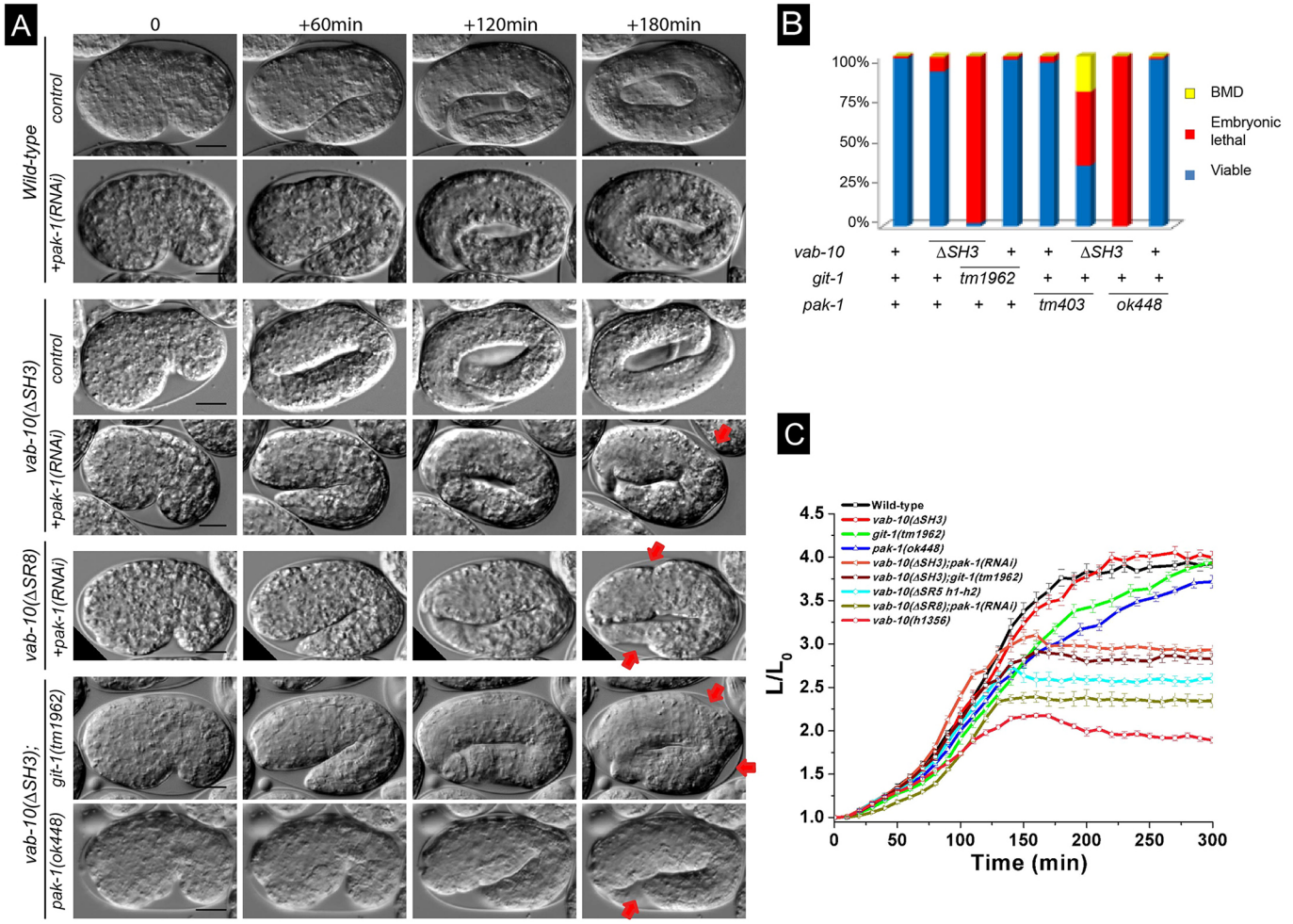

Fig. 3. Strong synergistic interactions between novel *vab-10* alleles and mutations affecting the mechanotransduction pathway. (A) DIC pictures showing the elongation of control embryos (row 1), *pak-1(RNAi)* embryos (row 2), *vab-10A(ΔSH3)* embryos (row 3), *vab-10A(ΔSH3)* embryos after *pak-1(RNAi)* (row 4), *vab-10A(ΔSR8); pak-1(RNAi)* embryos (row 5), *vab-10A(ΔSH3); git-1(tm1962)* embryos (row 6) and *vab-10A(ΔSH3); pak-1(ok448)* embryos (row 7). Pictures from rows 2, 4 and 6 are taken from Movies 1, 2 and 3, respectively. The time interval between images is indicated at the top. Red arrows indicate localized irregularity in the body wall. (B) Quantification of the embryonic and larval lethality in the double mutants shown in A; sample size was above 1300 individuals. (C) Elongation curves of the same double mutants (n=10 embryos for each genotype). Data are mean±s.e.m. Scale bars: 10 µm.

contract and relax, which recruits GIT-1 (Fig. 1C). To test which hemidesmosome component would be involved in recruiting GIT-1, and more specifically to explore whether the plakin domain could do so, we examined whether specific deletion of a plakin sub-domain or hemidesmosome component depletion affects the distribution of a novel GIT-1::GFP CRISPR knock-in.

In contrast to the severe GIT-1::GFP signal reduction observed in embryos defective for the essential muscle protein UNC-112 (Zhang et al., 2011) (Fig. 5A, bottom row), we found that absence of the SH3 domain did not affect the GIT-1::GFP signal (Fig. 5A, 2nd row). By contrast, absence of the first two helices of the SR5 domain partially reduced GIT-1 recruitment and strongly compromised hemidesmosome integrity where embryo curvature is the highest [Fig. 5A, line *vab-10(ΔSR5h1-h2)*], consistent with the global hemidesmosome detachment at that position (see Fig. 4C). As some GIT-1 remained at hemidesmosomes in *vab-10(ΔSR5h1-h2)* mutants, we tested whether other hemidesmosome proteins help recruit GIT-1 to hemidesmosomes by comparing the intensity and continuity along the anterior-posterior axis of the GIT-1 signal (Fig. 5B,B′) after RNAi-induced depletion of LET-805, VAB-10 or PAT-12, which are three essential hemidesmosome components (Zhang and Labouesse, 2010). We found that both parameters were reduced with the following grading in severity: *unc-112(RNAi)>let-805(RNAi)≥vab-10(RNAi)≈vab-10(ΔSR5h1-h2)≥pat-12(RNAi)* (Fig. 5C,D). In particular, a strong VAB-10 RNAi knockdown and the deletion of the first two helices of the SR5 domain resulted in very similar phenotypes, whereas *pat-12(RNAi)* moderately affected GIT-1::GFP levels and continuity, while still inducing a strong hemidesmosomal detachment defect (Fig. 5, see time +60 min). Importantly, loss of LET-805 does not significantly reduce VAB-10A levels (Hresko et al., 1999), suggesting that LET-805 might be directly involved in recruiting GIT-1. We conclude that GIT-1 recruitment is likely to involve LET-805 and potentially the VAB-10 SR5 domain.

To examine through another approach whether GIT-1 is indeed in close proximity to VAB-10, we used a bi-molecular fluorescence complementation (BiFC) strategy (Hu et al., 2002) (Fig. S3A). We generated CRISPR knock-in strains expressing GIT-1 linked at the C terminus to the 173 first residues of Venus, and VAB-10A linked at the C terminus to the last 83 residues of Venus. As a positive control, we co-expressed the same GIT-1::Venus(1-173) and a CRISPR-generated PIX-1::Venus(155-238), as vertebrate Git1 and

Development (2019) 146, dev183780. doi:10.1242/dev.183780

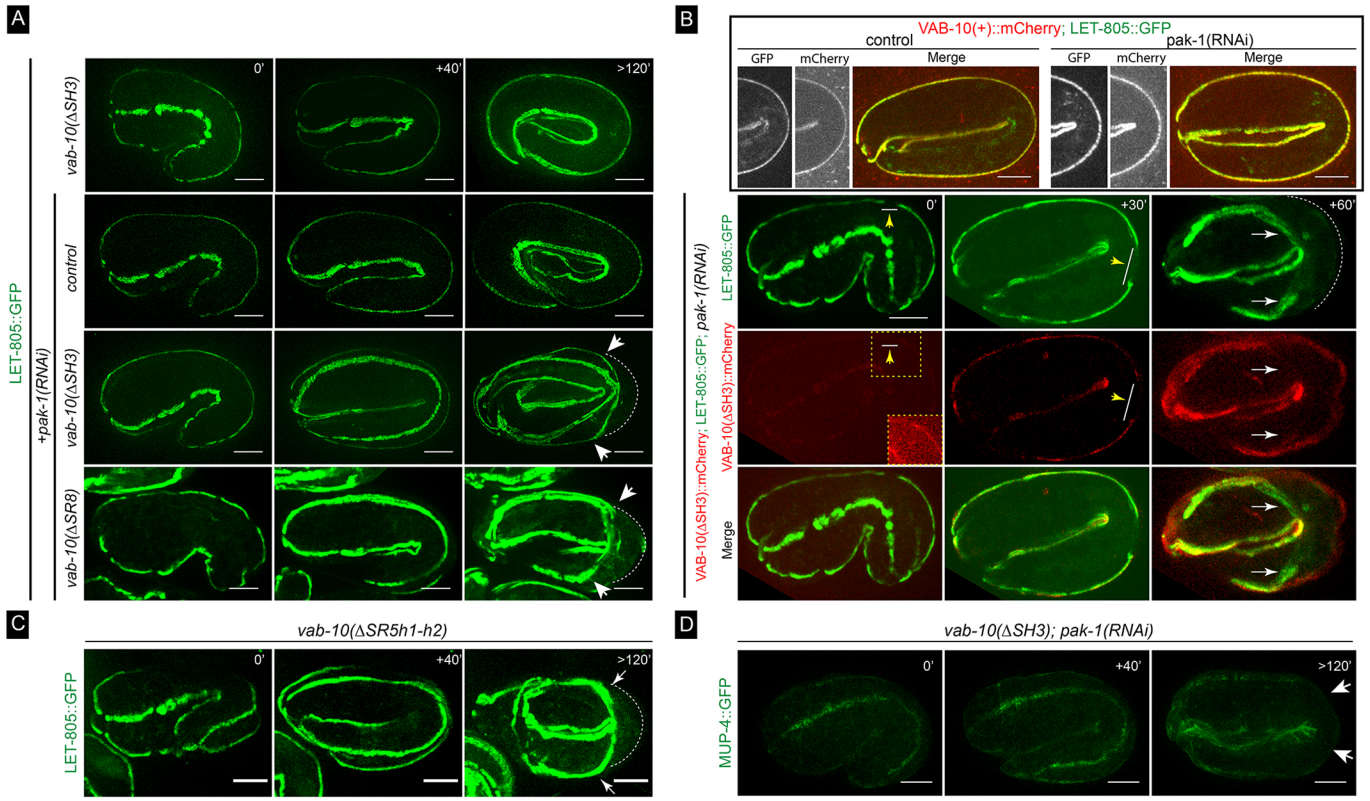

Fig. 4. The maintenance of hemidesmosome integrity requires multiple plakin sub-domains. Spinning disc fluorescence micrographs from time-lapse movies of embryos; each panel represents the projection of ~10-15 focal planes (out of generally 60). (A) Embryos homozygous for the CRISPR knock-in LET-805::GFP (*mc73*; *n*=35) with the genotype indicated on the left. In the *vab-10(ΔSH3); pak-1(RNAi)* embryo (3rd row) and the *vab-10(ΔSR8); pak-1(RNAi)* embryo (4th row), LET-805::GFP signal has detached from the body wall on the convex side and collapsed internally (white arrows, area of detachment; white dotted line, body wall – compare with 1st and 2nd rows). Pictures in rows 2 and 3 are from Movies 4 and 5, respectively. (B, row 1) Wild-type VAB-10(+)::mCherry; LET-805::GFP embryo alone or after *pak-1(RNAi)*; in both cases, the 1st panel shows the GFP signal in the turn of the embryo, the 2nd panel shows the mCherry channel and the 3rd panel shows the merge channel at the 2.1/2.2-fold stage. (B, rows 2-4) Embryo homozygous for *vab-10(mc62)::mCherry*; *LET-805::GFP(mc73), pak-1(RNAi)* at three different stages (the last being the 2.2-fold stage equivalent). This embryo displayed a small interruption in the hemidesmosome line visible at earlier stages (yellow arrow and line), which prefigured the area of detachment (white arrows); 20 out of 21 embryos showed detachment in the convex part, of which seven had a detectable interruption. 2nd row, LET-805::GFP signal; 3rd row, VAB-10(mc62)::mCherry signal (the inset corresponds to a small area for which the intensity was increased with FiJi); 4th row, merge. Pictures in row 4 are from Movie 6. (C) Embryo homozygous for *vab-10(ΔSR5h1-h2); LET-805::GFP*(*mc73*) (all embryos showed this phenotype; *n*=15). There is a detachment as in A rows 3 and 4 (arrows). (D) *vab-10(ΔSH3); pak-1(RNAi)* embryo homozygous for MUP-4::GFP knock-in (*mc121*; *n*=30). The MUP-4::GFP signal is much weaker on the convex side (between the white arrows). All examined embryos showed a detachment. Scale bars: 10 µm.

β-PIX form a complex (Frank and Hansen, 2008). We found that co-expressing GIT-1::Venus(1-173) with PIX-1::Venus(155-238) or VAB-10A::Venus(155-238) produced a clear hemidesmosomal signal (Fig. S3B) that was similar to that of endogenous VAB-10A and VAB-10B, and to that of our GIT-1::GFP knock-in (Fig. S3C,D). By contrast, embryos expressing only one Venus moiety failed to produce a signal (Fig. S3B). We conclude that VAB-10A and GIT-1 are located within less than 5-10 nm, the maximum distance beyond which a BiFC signal cannot be detected (Ciruela et al., 2010; Hu et al., 2002). As the fluorophore moieties were at the C terminus of each protein, and as VAB-10A is a large protein of 3400 residues, additional methods will be required to define whether GIT-1 directly interacts with VAB-10.

Biophysical evidence that the SH3 domain can be mechano-sensitive

The previous sections establish that the region shielding the SH3 domain of VAB-10 is essential for mechanotransduction, but that the SH3 domain is unlikely to directly interact with GIT-1. To explore how this region responds to force, we used molecular dynamics (MD) simulations. Our previous MD simulations of the homologous plakin domains from desmoplakin and plectin under a stretching force suggested that the SH3 domain mechanically stabilizes the spectrin repeats, and that force relieves the auto-inhibition of the SH3 domain by the preceding SR4 domain (Daday et al., 2017). This result, along with the 3D structure of plectin, predicted that the SH3 domain could have a mechanosensing role (Daday et al., 2017; Ortega et al., 2016).

We performed the same simulations for the model of VAB-10 shown in Fig. 1E (see Materials and Methods). Throughout our equilibrium MD simulations, the contact area between the SH3 domain and the rest of the protein was stable, with quartiles measuring 10.3-11.5 nm^2. This indicates that the VAB-10 SH3 domain interacts with the spectrin repeats like its desmoplakin and plectin homologues (Daday et al., 2017). To examine whether the SH3 domain might be mechano-sensitive, we subjected 10 snapshots from our equilibrium simulations to stretching forces acting on the termini in subsequent force-probe MD simulations. Similar to the tendencies observed for plectin, we found that the VAB-10 SR4 and SR5 domains always unfolded before the SH3

Development (2019) 146, dev183780. doi:10.1242/dev.183780

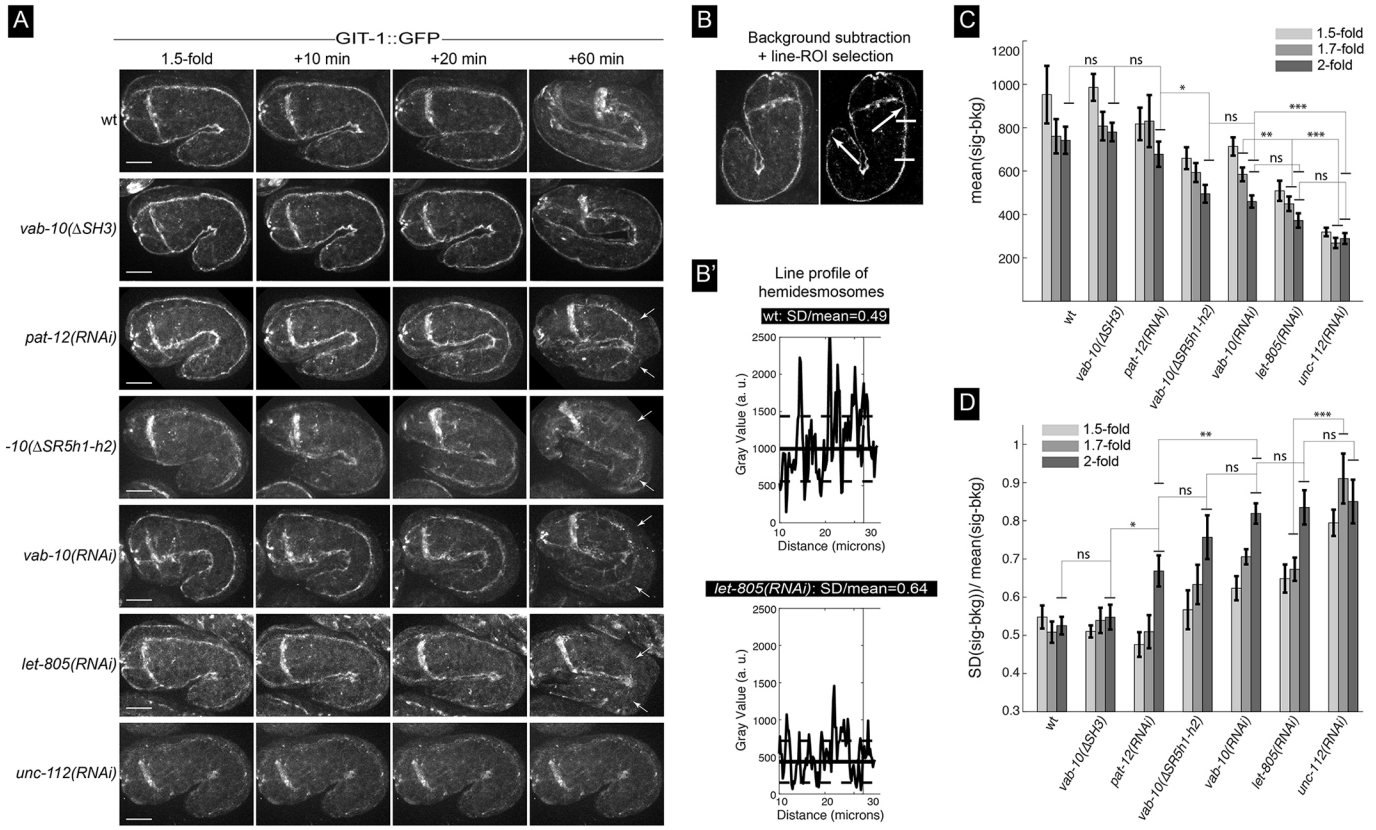

Fig. 5. Differential requirement of hemidesmosome components for GIT-1 recruitment. (A) Spinning disc fluorescence pictures from Movie 7 showing the distribution of the GIT-1::GFP knock-in (allele *mc86*) at the 1.5-fold stage and 10, 20 and 60 min later for the genetic backgrounds indicated on the left. Each picture shows only the top two hemidesmosomes. The hemidesmosome signal is collapsing internally from the most convex side of the embryo for *pat-12*, *vab-10* and *let-805* knockout embryos, as well as for *vab-10(ΔSR5h1-h2)* embryos (arrows). (B,B′) Procedure used for image analysis to quantify the signal intensity and continuity: after background subtraction (B), the signal intensity was measured along the hemidesmosome signal between the two arrows. (B′) Examples of the signal for two backgrounds, but just for the area between the short horizontal white lines in B. (C,D) Signal intensity (C) and continuity (D) for the backgrounds illustrated in A at three time points. Sample sizes were for 1.5-fold/1.7-fold/2-fold and older embryos: 8/12/11 (wild-type), 7/5/11 (*pat-12*), 6/6/6 (*mc62*), 9/9/9 (*mc64*), 13/14/14 (*vab-10*), 8/10/10 (*let-805*), 12/12/12 (*unc-112*). Scale bars: 10 µm. Data are mean±s.e.m. ns, not significant; **P*<0.5; ***P*<0.01; ****P*<0.001.

domain, i.e. the SH3 domain was invariably exposed and activated before its unfolding (Fig. S4A,B). This activation could happen through SR4 or SR5 unfolding (Fig. S4C). Hence, VAB-10 behaves like plectin and desmoplakin, which we examined in previous simulations. In the case of plectin, early activation after partial unfolding of just one SR, happened in about one-fifth of the simulations, while in the case of VAB-10, this happened even more frequently in one-third of cases (Fig. 6A). We also computationally analysed the plakin domain of VAB-10 carrying the Δ*SR5h1-h2* deletion, which removes the first two helices of the spectrin repeat shielding the SH3 domain. Our model predicts that the SH3 domain can still bind to the upstream SR4 (Fig. S4D), suggesting that the phenotype induced by this deletion is unlikely to result from the permanent availability of the SH3 domain for interaction with other proteins, and thus is unlikely to act as a constitutively active protein. Taken together, our results are compatible with the notion the VAB-10 SH3 domain can stabilize its plakin domain and potentially bind to other proteins if tension is exerted on the plakin region.

DISCUSSION

This study combines molecular genetic analysis of the *C. elegans* spectraplakin VAB-10/plectin with MD simulations to functionally test the function of its plakin domain. Our data establish that the SH3 domain with its shielding SR5 spectrin repeat, and the SR8 domain are essential to enable mechanotransduction at hemidesmosomes.

The recent crystal structure of the plakin domain of plectin revealed that this domain, which is composed of nine spectrin repeats, should adopt an extended rod-like shape (Ortega et al., 2011, 2016). Intriguingly, it also revealed the presence of an SH3 domain embedded within the central spectrin repeat (SR5). This SH3 is atypical inasmuch as it is missing several residues that normally ensure the interaction with Pro-rich target sequences within prototypical SH3 domains. Instead, it exhibits multiple interactions with the previous spectrin repeat SR4, challenging the notion that it could act as a bona fide SH3 domain, without excluding the possibility that it could interact with proteins in a non-canonic way (Ortega et al., 2011). By using the power of *C. elegans* molecular genetic tools and CRISPR-mediated recombination approaches, we could test the function of the VAB-10 plakin domain. Our key findings are that removal of the first two helices of the SR5 domain upstream of the SH3 domain induced highly penetrant embryonic elongation defects, but that deletion or point mutations within the SH3 domain, as well as deletion of the SR7 or SR8 domain, barely affected VAB-10 function on their own. Although, the SH3 domain is embedded within the SR5 domain, there are two arguments indicating that deletion of either domain results in phenotypes that are not due to some indirect secondary

Development (2019) 146, dev183780. doi:10.1242/dev.183780

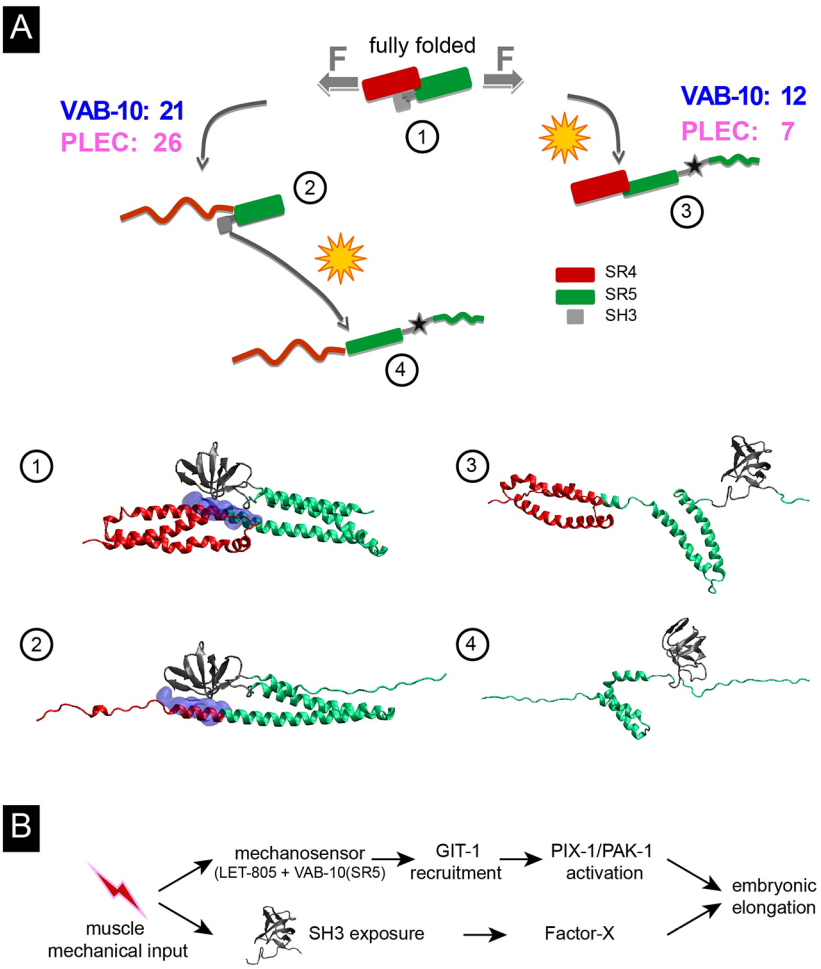

Fig. 6. Unfolding forces exerted on the plakin domain of VAB-10 unmask the SH3 domain. (A) Mechanical unfolding pathways of VAB-10 and plectin lead to SH3 activation. The numbers indicate how many trajectories showed SR4 unfolding first (left) versus SR5 unfolding first (right). Numbers for plectin are based on previous work (Daday et al., 2017). Red, SR4; green, SR5 (the thickness of the green rectangle is proportional to the number of helices contributing to it); blue, SH3-SR4 interface; grey, SH3; star, exposure; wavy red/green lines, unfolded SR helices. (B) Model for mechanotransduction at the hemidesmosome (see text).

mutation induced through the CRISPR approach. First, a complete SH3 deletion or deletion of the four residues PSVV within the SH3 domain resulted in a similar phenotype (Table 1). Second, previous staining of the strong *vab-10A(ju281)* embryos with a VAB-10A-specific antibody results in a similar hemidesmosome integrity defect in the most convex part of the embryo, as reported in Fig. 5 for *vab-10(ΔSR5h1-h2)* embryos (Bosher et al., 2003), consistent with Δ*SR5h1-h2* being a strong *vab-10* loss-of-function mutation. Furthermore, alterations of the SH3 domain, a SR8 deletion, but less frequently a SR7 deletion, induced embryonic elongation defects when combined with loss of the signalling proteins GIT-1 or PAK-1. The specificity of their phenotypes, and the observation that *vab-10(ΔSR5h1-h2)* deletion did not affect LET-805 distribution as much as the presumptive null allele *vab-10(h1356)*, strongly indicates that these deletions do not induce major structural defects in VAB-10 polypeptides but modify distinctive aspects of VAB-10 function.

The proteins GIT-1, PIX-1 and PAK-1 form the core of a mechanotransduction process induced by muscles in the epidermis to maintain hemidesmosome integrity when tension rises during elongation (Zhang et al., 2011). Genetically speaking, the synergistic effects observed between *vab-10(ΔSH3)* or *vab-10(ΔSR8)* deletions and *pak-1* or *git-1* mutations imply that the SH3 and SR8 domains are acting in a parallel rather than in a linear pathway with GIT-1/PAK-1 for hemidesmosome maintenance. Furthermore, these data predict that an unidentified Factor X acts in parallel to GIT-1/PIX-1/PAK-1 downstream of the mechanical input and the SH3 domain, which might either recruit or activate this Factor X (Fig. 6B). Finally, these genetic data also imply that neither the SH3 nor the SR8 domain is involved in recruiting GIT-1 to hemidesmosomes, consistent with our observations that GIT-1 was still present at hemidesmosomes in the absence of the SH3 domain. Instead, two arguments suggest that GIT-1 is recruited to hemidesmosomes at least in part through the interface between the SR5 domain and the presumptive hemidesmosome receptor LET-805. First, *vab-10(ΔSR5h1-h2)* deletion, and to a higher degree *let-805(RNAi)*, reduced GIT-1 level at hemidesmosomes. Second, their effect is unlikely to be indirect as LET-805::GFP levels remained high in *vab-10(ΔSR5h1-h2)* embryos (Fig. 4C), and as a *let-805* mutation does not reduce VAB-10A levels as monitored with the MH5 antibody against VAB-10A (Hresko et al., 1999). Our unpublished yeast 2-hybrid screens taking various parts of GIT-1 as baits, or conversely taking either the SR5 or the SH3 domains as baits, have failed to identify any significant prey. Although such negative results should be taken with care, failure might stem from the fact that the SR5-SH3 region, as well as GIT-1 interact only within a multi-protein complex that cannot be picked up through yeast 2-hybrid screens. A key objective for future studies will be to identify the predicted Factor X and the contact points between GIT-1 and hemidesmosome components.

How would proteins contributing to the mechanotransduction process assemble, and would they form a stable or a dynamic complex? Our MD simulations predicted that tension should expose the SH3 domain due to the unfolding of the SR4 and/or SR5

Development (2019) 146, dev183780. doi:10.1242/dev.183780

domains, as previously predicted for plectin and desmoplakin (Daday et al., 2017). As muscles repeatedly contract and relax (Lardennois et al., 2019; Zhang et al., 2011), one can speculate about various scenarios, which are not necessarily mutually exclusive. One possibility could be that a multi-protein signalling complex, including GIT-1 and Factor X, stably assembles along the VAB-10 plakin region once muscles contract; such a complex would fail to form in the absence of the SR5, SH3 or SR8 domains. Another possibility could be that the cyclic muscle-induced tension pattern promotes the transient and periodic recruitment of GIT-1 to the SR4-SR5 domains either in their folded or unfolded configuration. A third possibility would be that the SH3 domain recruits Factor X depending on tension, or in a more complex version that different signalling complexes alternatively bind and unbind to the SR4-bound SH3 and to the free SH3 to facilitate hemidesmosome remodelling. The discrepancy between the severity of the partial ΔSR5 deletion and the absence of any effect observed upon deletion of the SH3 domain alone is consistent with our MD simulations predicting that the partial SR5 deletion does not act by constitutively exposing the SH3 domain. It further suggests that the SR5 domain fulfils at least two roles: one related to the regulation of SH3 exposure following mechanical tension; and another corresponding to the binding of other proteins. Finally, the first part of the SR5 domain could be uniquely important for the correct folding of VAB-10. Interestingly, the SH3 domain of the plectin-1c isoform alone or more strongly in a presumptive SR4-SR5 folded configuration can bind microtubule-associated proteins to destabilize their interaction with microtubules (Valencia et al., 2013), implying that the SR4-SR5-SH3 region and the SH3 alone can interact with other proteins. Interestingly, we have previously reported that microtubule depletion in the *vab-10A(e698)* background leads to a phenotype very similar to that observed in the mutants described herein (Quintin et al., 2016).

The tension-dependent recruitment of GIT-1 and/or Factor X in some of these scenarios would posit VAB-10 as a mechanosensor. The paradigm for mechanosensing is largely based on talin and α-catenin, the two best-characterized mechanosensors. In both cases, it requires the unfolding of talin and α-catenin internal domains following their interaction with a junction receptor and with actin through terminal domains (del Rio et al., 2009; Hu et al., 2017; le Duc et al., 2010; Yao et al., 2016; Yao et al., 2014; Yonemura et al., 2010). There are two intriguing similarities between talin and plakins. One is that the plakin domain, much like the central part of talin, consists in several repeated domains (nine spectrin repeats versus 13 α helix bundles, respectively) that can be unfolded upon tension (Law et al., 2003; Lenne et al., 2000; Yao et al., 2016). Another is that among the bundles composing talin, the central repeat (R8) loops out of the preceding R7 and unfolds with it, which is partially reminiscent of the SH3 domain being inserted within the central SR5 domain of the plakin domain (Yao et al., 2016). Moreover, the Rho GTPase activating protein DLC1 (deleted in colorectal cancer 1) is active when bound to the folded R8 but inactive and unbound when R8 unfolds (Haining et al., 2018). These features may characterize ECM-linked mechanosensors.

As mentioned above, mechanosensing through talin requires it to bind to integrin and actin. In the case of VAB-10A, the situation would be conceptually similar although presumably molecularly different. As illustrated in Fig. 1B, there are two hemidesmosome-like structures in the epidermis, one basal and one apical, each associated with a different ECM. Both hemidesmosomes with their bridging intermediate filaments act as tendons linking muscles to the apical ECM. In the 3D space of embryos, when muscles contract in the anterior-posterior direction, this tendon-like structure oriented radially will come under high tension. Although not yet biochemically confirmed, genetic experiments suggest that VAB-10A should bind to the basal transmembrane receptor LET-805 (Bosher et al., 2003; Hresko et al., 1999; Zhang and Labouesse, 2010), much like plectin binds to β4-integrin through its two calponin-homology domains and probably the SR4-SR5-SH3 region (Frijns et al., 2012; Koster et al., 2004). Likewise, it is likely that VAB-10A can bind to MUP-4 on the apical side. While LET-805 basally and MUP-4 apically bear no homology to β4-integrin, their cytoplasmic tails are long enough to create multiple binding surfaces with VAB-10. Hence, when muscles exert tension on hemidesmosomes, the spectrin repeats of the VAB-10 plakin domain could unfold to expose its SH3 domain.

In conclusion, our work reveals the key role of the VAB-10 plakin domain in mediating mechanotransduction *in vivo*, and possibly mechanosensing. Molecular dynamics simulations suggest that the SH3 domain can alternate between an SR4-interacting state and a free state, with the latter being induced by force. Genetic analysis of *C. elegans* embryos suggests that the situation *in vivo* is complex and could involve multiple protein complexes acting in parallel. By extension, our data suggest that the SH3 domain and its shielding region are also likely to play a crucial signalling role *in vivo* in other spectraplakins.

MATERIALS AND METHODS

Strains and genetic analysis

Caenorhabditis elegans wild-type strain and transgenic animals derived from the *N2* strain were used for all experiments and maintained as described previously (Brenner, 1974). A complete list of strains and associated genotypes used in this study are included in Table S1. Data were collected over at least three separate sessions (except the entries *crt-1* and *mec-8* in Table 1B, which were over two sessions). Complementation tests were carried out by first establishing *vab-10A(ju281)/vab-10(new)* or *vab-10B(mc44)/vab-10(new)* trans-heterozygotes, which proved viable, then allowing such animals to lay eggs for a few hours. Lethality of the genotypes of the progeny was assessed over the next 2 days. The progeny of embryos segregating from the strain ML2594 [*vab-10(mc62[ΔSH3_820-873]/hT2 [bli-4(e937) let-?(q782) qIs48]I; pak-1(ok448)X*] was assessed in a similar way, except that the presumptive genotype of the progeny was defined by checking for the presence of a fluorescent signal corresponding to the balancer *qIs48* among unhatched embryos. Accordingly, we found that all unhatched GFP-negative embryos that had reached morphogenetic stages arrested as 2-F/2.5-fold (many *hT2* embryos arrest at an early-pre-morphogenetic stage).

Molecular biology and CRISPR/Cas9-mediated genome editing

Plasmid constructions were performed using a standard PCR method and general molecular biological techniques used as described by Sambrook et al. (1989). To construct knock-in DNA plasmid-based repair templates used for CRISPR/Cas9-mediated genome editing, we amplified the >1.5 kb upstream and >500 bp downstream sequences from the *N2* genomic DNA, and the fluorophore-encoding fragment from pre-existing vectors using Phusion DNA polymerase. PCR fragments were analysed on agarose gel and concentrated by either PCR clean-up or using a gel purification kit (QIAGEN) and their concentrations were measured using a Nanodrop (Eppendorf) before final assembly with pJET1.2 vector using NEBuilder HiFi DNA Assembly Cloning Kit (New England Biolabs). Small guide-encoding plasmids for CRISPR were generated by an overlap extension PCR method performed on the template pML2840, a version of the plasmid pIK198 (www.addgene.org/65629/) modified to easily insert the desired SG sequence (Table S2). To avoid Cas9 cleavage of the homologous repair template, the Cas9 site of the repair template was modified by introducing synonymous mutations either directly into the primers used for fragment amplification or separately using a Q5 site-directed mutagenesis kit (New England Biolabs). All DNA plasmids used for genome editing were

Development (2019) 146, dev183780. doi:10.1242/dev.183780

transformed into DH5α competent cells and subsequently purified by miniprep [PureLink Quick Plasmid Miniprep Kit (Thermo Fisher Scientific) or Plasmid Midi Kit (QIAGEN)]. All final DNA constructs were sequence verified before use. The sequences of sg-primers (Sigma) used in this study are included in Table S2.

Wild-type *N2 C. elegans* genetic background was used to generate *vab-10* CRISPR/Cas9 alleles; *let-805* and *mup-4* GFP knock-in strains were generated after injection in an *unc-119(ed3)* background (Dickinson et al., 2013). The sgRNA plasmid, knock-in repair template plasmid, Cas9-encoding plasmid and the appropriate co-injection marker (PRF4/myo-2::mCherry/myo-2::GFP) were co-injected into *N2* animals. Typically, injection mixes were prepared in DNase- and RNase-free MilliQ water and contained a combination of 50-100 ng/µl sgRNA plasmid (targeting specific gene), either 50 ng/µl repair template plasmid or 20-50 ng/µl ssDNA (PAGE-purified oligonucleotide) repair template, and co-injection markers pRF4 [rol-6 (su1006)] at 100 ng/µl and 2.5 ng/µl myo-2p::mCherry/myo-2p::GFP. Injection mixes were spun down in a microcentrifuge (Eppendorf) for at least 10-30 min at 20,000 ***g*** prior to use. Thirty to 40 young adult hermaphrodites were injected in the germline using an inverted micro-injection set up (Eppendorf). After injection, one animal per NGM food plate was dispatched and grown at 20°C for 2-3 days. F1 animals carrying co-injection markers were picked and singled out on separate NGM OP50 plates, and grown at 20°C until eggs or larvae were spotted. Each F1 mother was lysed in a separate PCR tube and standard worm PCR protocol was followed using appropriate pairs of primers (annealing in the inserted sequence and a genomic region not included in the repair template). For the construction of some transgenic strains, we also used Co-CRISPR the *dpy-10* phenotype (Paix et al., 2015) or integration of a self-excisable cassette carrying a visible marker (Dickinson et al., 2015) method. All genotyping experiments were carried out using standard worm PCR methods (Table S2) (Ahringer, 2006). Confirmed alleles were sequenced and verified (Eurofins).

RNA-mediated interference (RNAi)

RNAi experiments were performed either by feeding on *HT115 Escherichia coli* bacteria strains generating double-stranded RNA (dsRNA) targeting genes of interest or by injection of *in vitro* synthesized double-stranded RNA on young L4 stage of the animals. Feeding RNAi clones for *crt-1* and *mec-8* were used from the Ahringer-MRC feeding RNA interference (RNAi) library (Kamath et al., 2003). RNAi feeding was performed using standard procedures, with 100 µg ml^{-1} ampicillin/1 mM IPTG (Sigma). Empty L4440 RNAi vector served as a control. Other experiments involving RNAi were carried out by injection of dsRNA.

To generate dsRNA for the injection, genomic fragments were PCR amplified using Phusion DNA polymerase (ThermoFisher) and these fragments further served as templates for *in vitro* dsRNA synthesis using T3 or T7 mMESSAGE mMACHINE Kit (Ambion). For gene knockdown experiments by feeding, L4/L1 hermaphrodites were grown on RNAi plates for 24-36 h; for dsRNA injection, 20-30 young L4 hermaphrodites were injected with dsRNA targeting gene of interests and grown for 14-20 h prior to experiments.

Spinning disk and Nomarski microscopy

For live imaging, embryos were picked from NGM plate by mouth pipette, washed thoroughly in M9 medium and mounted on 2-5% agarose pads after sealing the slides with paraffin oil. Spinning disk imaging of embryos was performed using a Roper Scientific spinning disk system (Zeiss Axio Observer Z1 microscope, Yokogawa CSUX1-A1 spinning disk confocal head, Photometrics Evolve 512 EMCCD camera, Metamorph software) equipped with a 63× and 100× oil-immersion objective, NA=1.4. The temperature of the microscopy room was maintained at 20°C. Images of embryos were acquired in either streaming mode with 100 ms exposure or time-lapse mode with 100 ms exposure and at 5 min intervals. Laser power and exposure times were kept constant throughout the experiments for specific strains and their control genotypes. For the quantification of hemidesmosomes, images were acquired with 100 ms exposure time in stream mode with 0.3 µm step size. Images were processed and quantified using FIJI. Fluorophores used in this study include eGFP, GFP (65C), mCherry and split VENUS.

Time-lapse DIC movies were acquired using a Leica DMI6000 upright microscope, a 40× or 63× oil-immersion objective NA=1.25 and a Photometrics Coolsnap HQ2 camera placed in the temperature-controlled room at 20°C; acquisitions were carried out in at least two sessions. For *C. elegans* larvae image acquisition, animals were anesthetized using 0.1 mmol/l levamisole in M9 buffer and mounted on 2% agarose pad.

Homology modelling

We used MODELLER (Šali and Blundell, 1993) (version 9.14) through the interface in UCSF Chimera version 1.12 (Pettersen et al., 2004) for homology modelling. Currently, two crystal structures of proteins with SH3 insertions are available: 3PE0 (plectin) and 3R6N (desmoplakin). The main difference between these two structures is the presence of a small helix, B0, in spectrin repeat 5. Given that a later investigation found no such small helix in plectin (Ortega et al., 2016), we chose to model VAB-10 using 3R6N (desmoplakin), despite the fact that the sequence identity is lower (27.37% for desmoplakin as opposed to 32.10%). When compared with 3R6N, the obtained model has a distance of 0.46 Å between the 265 pairs of Cα atoms within 2.0 Å of each other out of a total of 274 pairs. As given by MODELLER's estimates, the homology model is at an RMSD of 2.21 Å and an overlap of Cα atoms of 0.91 within 3.5 Å. We compared the three structures (3PE0, 3R6N and our obtained homology model) in Fig. 1E. We also obtained homology models for the mutant protein VAB-10(mc64) lacking the first two helices of SR5, which show the SH3 domain still associated to helix 2C, but helix 3C is shown to loop back onto the rest of the structure in two different conformations (Fig. S3D).

Molecular dynamics simulations

We followed the same protocol as described in our previous work (Daday et al., 2017). In short, we used the Amber99SB-ILDN* force field (Liu et al., 2016) with a TIP3P water model (Jorgensen et al., 1983) and virtual sites (Berendsen and van Gunsteren, 1984), allowing for a 5 fs time step. All MD simulations were performed using GROMACS version 5.0 (Pronk et al., 2013). We performed equilibrium molecular dynamics on ∼190 K atoms in a dodecahedron box for 1 µs, and thereafter we chose the top 10 frames through cluster analysis between 100 and 1000 ns, with a cutoff of 0.088 nm. These 10 frames were later used for force-probe simulations. Ten simulations were performed at each of the velocities 1, 1/3 and 1/10 nm/ns, and three simulations were performed at a velocity of 1/30 nm/ns. All other parameters were identical to the procedure described in our previous work, in particular for the re-solvation procedure for plectin. The equilibrium molecular dynamics simulation shows a backbone RMSD with an inter-quantile range between 3.4 and 4.4 Å. The helicity of the construct is very stable, with quartiles at 209 and 214 residues out of the 274 in our structure, and the β-strand content is stable, with quartiles at 35 and 40 residues, and a small positive drift (one more residue in strands every 236 ns). Overall, we consider the homology model to be a good representation of this region of VAB-10.

Image processing, quantification and statistical analysis

Images in Fig. 5 were analysed as follows: the background was estimated by Gaussian filter of the original image with a width of 30 pixel; the background image was subtracted from the original one; the line profile of the GIT-1 signal along the hemidesmosomes was measured on the subtracted image. We recorded two observables from the line profile: the average signal and its standard deviation. The average signal is shown in Fig. 5C, whereas the ratio between standard deviation and average signal (coefficient of variation) is shown in Fig. 5D as a measure of the discontinuity. Indeed a fragmented signal shows higher relative fluctuations. All images were analysed using ImageJ (FiJi) software (rsb.info.nih.gov/ij/) and statistical tests were performed using MATLAB R2018b (MathWorks). For Fig. 5 a Wilcoxon test was used, whereas for Fig. 2J a χ^2 test was applied.

Acknowledgements

We thank the *Caenorhabditis* Genetics Center (funded by the NIH Office of Research Infrastructure Programs P40 OD010440) for strains, the IBPS Imaging Facility for advice and Kelly Molnar for English proofreading.

Competing interests
The authors declare no competing or financial interests.

Author contributions
Conceptualization: S.K.S., M.L.; Methodology: S.K.S., C.D., F.G., M.L.; Software: C.D., T.F.; Formal analysis: C.D., T.F.; Investigation: S.K.S., T.V.-B.; Resources: S.T., S.Q.; Writing - original draft: M.L.; Writing - review & editing: S.K.S., T.V.-B., S.Q.; Visualization: S.K.S.; Supervision: F.G., M.L.; Project administration: M.L.; Funding acquisition: F.R., F.G., M.L.

Funding
This work was supported by the European Research Council (294744), by the Agence Nationale de la Recherche (ANR-11-BSV2-0023), and by installation funds from the Centre National de la Recherche Scientifique and Université Pierre et Marie Curie to M.L. This work was also made possible by institutional funds from the Centre National de la Recherche Scientifique, the University of Strasbourg and the Université Pierre et Marie Curie, as well as by the Labex grant ANR-10-LABX-0030-INRT, which is a French State fund managed by the Agence Nationale de la Recherche under the framework programme Investissements d'Avenir labelled ANR-10-IDEX-0002-02 to the Institut de Génétique et de Biologie Moléculaire et Cellulaire. F.G. acknowledges funding from the Klaus Tschira Stiftung, from the Deutsche Forschungsgemeinschaft through the priority programme SPP1782, and from the state of Baden-Württemberg and the Deutsche Forschungsgemeinschaft through grant INST 35/1134-1 FUGG.

Supplementary information
Supplementary information available online at
http://dev.biologists.org/lookup/doi/10.1242/dev.183780.supplemental

Peer review history
The peer review history is available online at https://dev.biologists.org/lookup/doi/10.1242/dev.183780.reviewer-comments.pdf.

References
Ahringer, J. (2006). Reverse genetics. *In WormBook, (ed*. The *C. elegans* Research Community), pp. 1-43: WormBook. doi/10.1895/wormbook.1.47.1
Aigouy, B., Farhadifar, R., Staple, D. B., Sagner, A., Röper, J.-C., Jülicher, F. and Eaton, S. (2010). Cell flow reorients the axis of planar polarity in the wing epithelium of Drosophila. *Cell* **142**, 773-786. doi:10.1016/j.cell.2010.07.042
Almeida, F. V., Walko, G., McMillan, J. R., McGrath, J. A., Wiche, G., Barber, A. H. and Connelly, J. T. (2015). The cytolinker plectin regulates nuclear mechanotransduction in keratinocytes. *J. Cell Sci.* **128**, 4475-4486. doi:10.1242/jcs.173435
Berendsen, H. J. C. and van Gunsteren, W. F. (1984). Molecular dynamics simulations: techniques and approaches. In *On Molecular Liquids — Dynamics and Interactions*, Vol. C135 (ed. A. J. Barnes, W. J. Orville-Thomas and J. Yarwood), pp. 475-500. Dordrecht: Reidel. NATO ASI Series.
Bosher, J. M., Hahn, B.-S., Legouis, R., Sookhareea, S., Weimer, R. M., Gansmuller, A., Chisholm, A. D., Rose, A. M., Bessereau, J.-L. and Labouesse, M. (2003). The *Caenorhabditis elegans vab*-10 spectraplakin isoforms protect the epidermis against internal and external forces. *J. Cell Biol.* **161**, 757-768. doi:10.1083/jcb.200302151
Brenner, S. (1974). The genetics of Caenorhabditis elegans. *Genetics* **77**, 71-94.
Chen, Y., Ju, L., Rushdi, M., Ge, C. and Zhu, C. (2017). Receptor-mediated cell mechanosensing. *Mol. Biol. Cell* **28**, 3134-3155. doi:10.1091/mbc.e17-04-0228
Choi, H.-J. and Weis, W. I. (2011). Crystal structure of a rigid four-spectrin-repeat fragment of the human desmoplakin plakin domain. *J. Mol. Biol.* **409**, 800-812. doi:10.1016/j.jmb.2011.04.046
Ciruela, F., Vilardaga, J.-P. and Fernández-Dueñas, V. (2010). Lighting up multiprotein complexes: lessons from GPCR oligomerization. *Trends Biotechnol.* **28**, 407-415. doi:10.1016/j.tibtech.2010.05.002
Collinet, C., Rauzi, M., Lenne, P.-F. and Lecuit, T. (2015). Local and tissue-scale forces drive oriented junction growth during tissue extension. *Nat. Cell Biol.* **17**, 1247-1258. doi:10.1038/ncb3226
Daday, C., Kolšek, K. and Gräter, F. (2017). The mechano-sensing role of the unique SH3 insertion in plakin domains revealed by Molecular Dynamics simulations. *Sci. Rep.* **7**, 11669. doi:10.1038/s41598-017-11017-2
del Rio, A., Perez-Jimenez, R., Liu, R., Roca-Cusachs, P., Fernandez, J. M. and Sheetz, M. P. (2009). Stretching single talin rod molecules activates vinculin binding. *Science* **323**, 638-641. doi:10.1126/science.1162912
Dickinson, D. J., Ward, J. D., Reiner, D. J. and Goldstein, B. (2013). Engineering the Caenorhabditis elegans genome using Cas9-triggered homologous recombination. *Nat. Methods* **10**, 1028-1034. doi:10.1038/nmeth.2641
Dickinson, D. J., Pani, A. M., Heppert, J. K., Higgins, C. D. and Goldstein, B. (2015). Streamlined genome engineering with a self-excising drug selection cassette. *Genetics* **200**, 1035-1049. doi: 10.1534/genetics.115.178335
Francis, R. and Waterston, R. H. (1991). Muscle cell attachment in Caenorhabditis elegans. *J. Cell Biol.* **114**, 465-479. doi:10.1083/jcb.114.3.465
Frank, S. R. and Hansen, S. H. (2008). The PIX-GIT complex: a G protein signaling cassette in control of cell shape. *Semin. Cell Dev. Biol.* **19**, 234-244. doi:10.1016/j.semcdb.2008.01.002
Frijns, E., Kuikman, I., Litjens, S., Raspe, M., Jalink, K., Ports, M., Wilhelmsen, K. and Sonnenberg, A. (2012). Phosphorylation of threonine 1736 in the C-terminal tail of integrin beta4 contributes to hemidesmosome disassembly. *Mol. Biol. Cell* **23**, 1475-1485. doi:10.1091/mbc.e11-11-0957
Gieseler, K., Qadota, H. and Benian, G. M. (2017). Development, structure, and maintenance of C. elegans body wall muscle. *WormBook* **2017**, 1-59. doi:10.1895/wormbook.1.81.2
Gilmour, D., Rembold, M. and Leptin, M. (2017). From morphogen to morphogenesis and back. *Nature* **541**, 311-320. doi:10.1038/nature21348
Haining, A. W. M., Rahikainen, R., Cortes, E., Lachowski, D., Rice, A., von Essen, M., Hytönen, V. P. and Del Río Hernández, A. (2018). Mechanotransduction in talin through the interaction of the R8 domain with DLC1. *PLoS Biol.* **16**, e2005599. doi:10.1371/journal.pbio.2005599
Hresko, M. C., Schriefer, L. A., Shrimankar, P. and Waterston, R. H. (1999). Myotactin, a novel hypodermal protein involved in muscle-cell adhesion in *Caenorhabditis elegans*. *J. Cell Biol.* **146**, 659-672. doi:10.1083/jcb.146.3.659
Hu, C.-D., Chinenov, Y. and Kerppola, T. K. (2002). Visualization of interactions among bZIP and Rel family proteins in living cells using bimolecular fluorescence complementation. *Mol. Cell* **9**, 789-798. doi:10.1016/S1097-2765(02)00496-3
Hu, X., Margadant, F. M., Yao, M. and Sheetz, M. P. (2017). Molecular stretching modulates mechanosensing pathways. *Protein Sci.* **26**, 1337-1351. doi:10.1002/pro.3188
Iskratsch, T., Wolfenson, H. and Sheetz, M. P. (2014). Appreciating force and shape-the rise of mechanotransduction in cell biology. *Nat. Rev. Mol. Cell Biol.* **15**, 825-833. doi:10.1038/nrm3903
Jorgensen, W. L., Chandrasekhar, J. and Madura, J. D. (1983). Comparison of simple potential functions for simulating liquid water. *J. Chem. Phys.* **79**, 926-935. doi:10.1063/1.445869
Kamath, R. S., Fraser, A. G., Dong, Y., Poulin, G., Durbin, R., Gotta, M., Kanapin, A., Le Bot, N., Moreno, S., Sohrmann, M. et al. (2003). Systematic functional analysis of the *Caenorhabditis elegans* genome using RNAi. *Nature* **421**, 231-237.
Koster, J., van Wilpe, S., Kuikman, I., Litjens, S. H. M. and Sonnenberg, A. (2004). Role of binding of plectin to the integrin beta4 subunit in the assembly of hemidesmosomes. *Mol. Biol. Cell* **15**, 1211-1223. doi:10.1091/mbc.e03-09-0697
Ladoux, B., Nelson, W. J., Yan, J. and Mège, R. M. (2015). The mechanotransduction machinery at work at adherens junctions. *Integr. Biol.* **7**, 1109-1119. doi:10.1039/c5ib00070j
Lardennois, A., Pásti, G., Ferraro, T., Llense, F., Mahou, P., Pontabry, J., Rodriguez, D., Kim, S., Ono, S., Beaurepaire, E. et al. (2019). An actin-based viscoplastic lock ensures progressive body-axis elongation. *Nature* **573**, 266-270. doi:10.1038/s41586-019-1509-4
Law, R., Carl, P., Harper, S., Dalhaimer, P., Speicher, D. W. and Discher, D. E. (2003). Cooperativity in forced unfolding of tandem spectrin repeats. *Biophys. J.* **84**, 533-544. doi:10.1016/S0006-3495(03)74872-3
le Duc, Q., Shi, Q., Blonk, I., Sonnenberg, A., Wang, N., Leckband, D. and de Rooij, J. (2010). Vinculin potentiates E-cadherin mechanosensing and is recruited to actin-anchored sites within adherens junctions in a myosin II-dependent manner. *J. Cell Biol.* **189**, 1107-1115. doi:10.1083/jcb.201001149
Lenne, P.-F., Raae, A. J., Altmann, S. M., Saraste, M. and Hörber, J. K. H. (2000). States and transitions during forced unfolding of a single spectrin repeat. *FEBS Lett.* **476**, 124-128. doi:10.1016/S0014-5793(00)01704-X
Liu, A. S., Wang, H., Copeland, C. R., Chen, C. S., Shenoy, V. B. and Reich, D. H. (2016). Matrix viscoplasticity and its shielding by active mechanics in microtissue models: experiments and mathematical modeling. *Sci. Rep.* **6**, 33919. doi:10.1038/srep33919
Lye, C. M., Blanchard, G. B., Naylor, H. W., Muresan, L., Huisken, J., Adams, R. J. and Sanson, B. (2015). Mechanical coupling between endoderm invagination and axis extension in Drosophila. *PLoS Biol.* **13**, e1002292. doi:10.1371/journal.pbio.1002292
Moore, S. W., Roca-Cusachs, P. and Sheetz, M. P. (2010). Stretchy proteins on stretchy substrates: the important elements of integrin-mediated rigidity sensing. *Dev. Cell* **19**, 194-206. doi:10.1016/j.devcel.2010.07.018
Ortega, E., Buey, R. M., Sonnenberg, A. and de Pereda, J. M. (2011). The structure of the plakin domain of plectin reveals a non-canonical SH3 domain interacting with its fourth spectrin repeat. *J. Biol. Chem.* **286**, 12429-12438. doi:10.1074/jbc.M110.197467
Ortega, E., Manso, J. A., Buey, R. M., Carballido, A. M., Carabias, A., Sonnenberg, A. and de Pereda, J. M. (2016). The structure of the Plakin domain of Plectin reveals an extended rod-like shape. *J. Biol. Chem.* **291**, 18643-18662. doi:10.1074/jbc.M116.732909
Paix, A., Folkmann, A., Rasoloson, D. and Seydoux, G. (2015). High efficiency, homology-directed genome editing in Caenorhabditis elegans using CRISPR-Cas9 ribonucleoprotein complexes. *Genetics* **201**, 47-54. doi: 10.1534/genetics
Pettersen, E. F., Goddard, T. D., Huang, C. C., Couch, G. S., Greenblatt, D. M., Meng, E. C. and Ferrin, T. E. (2004). UCSF Chimera–a visualization system for

exploratory research and analysis. *J. Comput. Chem.* **25**, 1605-1612. doi:10.1002/jcc.20084

Pronk, S., Páll, S., Schulz, R., Larsson, P., Bjelkmar, P., Apostolov, R., Shirts, M. R., Smith, J. C., Kasson, P. M., van der Spoel, D. et al. (2013). GROMACS 4.5: a high-throughput and highly parallel open source molecular simulation toolkit. *Bioinformatics* **29**, 845-854. doi:10.1093/bioinformatics/btt055

Quintin, S., Wang, S., Pontabry, J., Bender, A., Robin, F., Hyenne, V., Landmann, F., Gally, C., Oegema, K. and Labouesse, M. (2016). Non-centrosomal epidermal microtubules act in parallel to LET-502/ROCK to promote C. elegans elongation. *Development* **143**, 160-173. doi:10.1242/dev.126615

Šali, A. and Blundell, T. L. (1993). Comparative protein modelling by satisfaction of spatial restraints. *J. Mol. Biol.* **234**, 779-815. doi:10.1006/jmbi.1993.1626

Sambrook, J., Fritsch, E. F. and Maniatis, T. (1989). *Molecular Cloning: A Laboratory Manual*. Cold Spring Harbor, NY: Cold Spring Harbor Laboratory Press.

Sawada, Y. and Sheetz, M. P. (2002). Force transduction by Triton cytoskeletons. *J. Cell Biol.* **156**, 609-615. doi:10.1083/jcb.200110068

Sawada, Y., Tamada, M., Dubin-Thaler, B. J., Cherniavskaya, O., Sakai, R., Tanaka, S. and Sheetz, M. P. (2006). Force sensing by mechanical extension of the Src family kinase substrate p130Cas. *Cell* **127**, 1015-1026. doi:10.1016/j.cell.2006.09.044

Sonnenberg, A. and Liem, R. K. H. (2007). Plakins in development and disease. *Exp. Cell Res.* **313**, 2189-2203. doi:10.1016/j.yexcr.2007.03.039

Takawira, D., Budinger, G. R. S., Hopkinson, S. B. and Jones, J. C. R. (2011). A dystroglycan/plectin scaffold mediates mechanical pathway bifurcation in lung epithelial cells. *J. Biol. Chem.* **286**, 6301-6310. doi:10.1074/jbc.M110.178988

Valencia, R. G., Walko, G., Janda, L., Novacek, J., Mihailovska, E., Reipert, S., Andrä-Marobela, K. and Wiche, G. (2013). Intermediate filament-associated cytolinker plectin 1c destabilizes microtubules in keratinocytes. *Mol. Biol. Cell* **24**, 768-784. doi:10.1091/mbc.e12-06-0488

Vuong-Brender, T. T. K., Yang, X. and Labouesse, M. (2016). C. elegans embryonic morphogenesis. *Curr. Top. Dev. Biol.* **116**, 597-616. doi:10.1016/bs.ctdb.2015.11.012

Yao, M., Qiu, W., Liu, R., Efremov, A. K., Cong, P., Seddiki, R., Payre, M., Lim, C. T., Ladoux, B., Mège, R.-M. et al. (2014). Force-dependent conformational switch of alpha-catenin controls vinculin binding. *Nat. Commun.* **5**, 4525. doi:10.1038/ncomms5525

Yao, M., Goult, B. T., Klapholz, B., Hu, X., Toseland, C. P., Guo, Y., Cong, P., Sheetz, M. P. and Yan, J. (2016). The mechanical response of talin. *Nat. Commun.* **7**, 11966. doi:10.1038/ncomms11966

Yonemura, S., Wada, Y., Watanabe, T., Nagafuchi, A. and Shibata, M. (2010). alpha-Catenin as a tension transducer that induces adherens junction development. *Nat. Cell Biol.* **12**, 533-542. doi:10.1038/ncb2055

Zahreddine, H., Zhang, H., Diogon, M., Nagamatsu, Y. and Labouesse, M. (2010). CRT-1/calreticulin and the E3 ligase EEL-1/HUWE1 control hemidesmosome maturation in *C.* elegans development. *Curr. Biol.* **20**, 322-327. doi:10.1016/j.cub.2009.12.061

Zhang, H. and Labouesse, M. (2010). The making of hemidesmosome structures in vivo. *Dev. Dyn.* **239**, 1465-1476. doi:10.1002/dvdy.22255

Zhang, H., Landmann, F., Zahreddine, H., Rodriguez, D., Koch, M. and Labouesse, M. (2011). A tension-induced mechanotransduction pathway promotes epithelial morphogenesis. *Nature* **471**, 99-103. doi:10.1038/nature09765

Zhang, J., Yue, J. and Wu, X. (2017). Spectraplakin family proteins - cytoskeletal crosslinkers with versatile roles. *J. Cell Sci.* **130**, 2447-2457. doi:10.1242/jcs.196154